# X-ray Absorption Spectroscopy of Mn/Co/$TiO_2$ Fischer−Tropsch Catalysts: Relationships between Preparation Method, Molecular Structure, and Catalyst Performance

**Fernando Morales, Didier Grandjean, Ad Mens, Frank M. F. de Groot, and Bert M. Weckhuysen***

*Inorganic Chemistry and Catalysis, Department of Chemistry, Utrecht University, Sorbonnelaan 16, 3584 CA Utrecht, The Netherlands*

*Received: November 15, 2005; In Final Form: March 2, 2006*

The effects of the addition of manganese to a series of $TiO_2$-supported cobalt Fischer−Tropsch (FT) catalysts prepared by different methods were studied by a combination of X-ray diffraction (XRD), temperature-programmed reduction (TPR), transmission electron microscopy (TEM), and in situ X-ray absorption fine structure (XAFS) spectroscopy at the Co and Mn K-edges. After calcination, the catalysts were generally composed of large $Co_3O_4$ clusters in the range 15−35 nm and a $MnO_2$-type phase, which existed either dispersed on the $TiO_2$ surface or covering the $Co_3O_4$ particles. Manganese was also found to coexist with the $Co_3O_4$ in the form of $Co_{3-x}Mn_xO_4$ solutions, as revealed by XRD and XAFS. Characterization of the catalysts after $H_2$ reduction at 350 °C by XAFS and TEM showed mostly the formation of very small $Co^0$ particles (around 2−6 nm), indicating that the cobalt phase tends to redisperse during the reduction process from $Co_3O_4$ to $Co^0$. The presence of manganese was found to hamper the cobalt reducibility, with this effect being more severe when $Co_{3-x}Mn_xO_4$ solutions were initially present in the catalyst precursors. Moreover, the presence of manganese generally led to the formation of larger cobalt agglomerates (∼8−15 nm) upon reduction, probably as a consequence of the decrease in cobalt reducibility. The XAFS results revealed that all reduced catalysts contained manganese entirely in a $Mn^{2+}$ state, and two well-distinguished compounds could be identified: (1) a highly dispersed $Ti_2MnO_4$-type phase located at the $TiO_2$ surface and (2) a less dispersed MnO phase being in the proximity of the cobalt particles. Furthermore, the MnO was also found to exist partially mixed with a CoO phase in the form of rock-salt $Mn_{1-x}Co_xO$-type solid solutions. The existence of the later solutions was further confirmed by scanning transmission electron microscopy with electron energy loss spectroscopy (STEM-EELS) for a Mn-rich sample. Finally, the cobalt active site composition in the catalysts after reduction at 300 and 350 °C was linked to the catalytic performances obtained under reaction conditions of 220 °C, 1 bar, and $H_2/CO = 2$. The catalysts with larger $Co^0$ particles (∼ >5 nm) and lower Co reduction extents displayed a higher intrinsic hydrogenation activity and a longer catalyst lifetime. Interestingly, the MnO and $Mn_{1-x}Co_xO$ species effectively promoted these larger $Co^0$ particles by increasing the $C_{5+}$ selectivity and decreasing the $CH_4$ production, while they did not significantly influence the selectivity of the catalysts containing very small $Co^0$ particles.

## Introduction

An increasing demand for clean fuels and chemicals is expected to lead to an important shift from crude oil to natural gas as feedstock for chemical industries. This will certainly involve the use of Fischer−Tropsch (FT) technology, in which high molecular weight hydrocarbons are synthesized by catalytic hydrogenation of CO using Co-based catalysts.[1,2] Subsequent hydrocracking of the waxes leads to clean middle distillates such as diesel fuels, chemicals, naphtha, and lubricants. The increased efficiencies in the FT process, the ability to build large-scale plants to capture economies of scale, and the high crude oil price have made gas-to-liquid (GTL) technology attractive and competitive to the current crude oil refinery industries.[3−5]

It is well-known that the FT catalytic properties of supported cobalt catalysts are known to be largely dependent on both the cobalt reduction extent and size of the $Co^0$ crystallites formed upon catalyst activation. For this reason, many studies have aimed to establish clear relationships between the cobalt active site distributions and their FT catalytic performances. In the early 1980s, it was reported that CO hydrogenation at 1 bar on $Co/Al_2O_3$ catalysts is structure-sensitive,[6] since it was possible to correlate (1) an increasing turnover rate with a decreasing $Co^0$ dispersion and (2) the variations in selectivity with changes in the rate of chain termination relative to the rate of chain propagation. Nonetheless, the possibility that unreduced cobalt present at the catalyst surface would account for the changes in activity and selectivity could not be ruled out. In other work,[7] it was reported that cobalt reduction extent plays an important role in CO hydrogenation over $Al_2O_3$-supported cobalt catalysts, since higher turnover frequencies were observed for catalysts with a lower reduction extent.

Iglesia and co-workers have claimed that the FT synthesis is a structural-insensitive reaction for supported cobalt catalysts with dispersions between 0.45 to 9.5%, corresponding to particle sizes of 230 and 10 nm, respectively.[8] Within this dispersion range, the reactivity of surface Co atoms in the FT synthesis is not influenced by the size or chemical identity of the metal oxide support, and hence, it is expected that a catalyst would yield

* To whom correspondence should be addressed. E-mail: b.m.weckhuysen@chem.uu.nl.

10.1021/jp0565958 CCC: $33.50 
Published on Web 04/08/2006

activities as a function of the number of available $Co^0$ sites. However, structural changes of the cobalt particles during the FT synthesis may result in a variation of the number of available sites.[9,10] The structural changes during FT operation may include the transformation of metallic cobalt, to cobalt oxides and/or cobalt carbides, and the sintering or segregation of the particles. Another possible cause of deactivation may be the loss of active phase as a result of the occurrence of strong-metal support interactions (SMSIs). SMSIs have been shown to occur in $TiO_2$-supported Co catalysts at high temperatures, at which $TiO_2$ may be reduced to $TiO_x$, which can migrate onto the surface of the $Co^0$ particles, causing a blockage of the active sites and thus a decrease of CO adsorption.[11,12] Similar SMSI effects are also expected to occur when an excess of oxide promoter is employed, for example, in the case of transition metal oxides. These promoters may exhibit a similar mobility toward the cobalt surface leading to the poisoning and deactivation of small supported particles.

The use of manganese as a promoter for Co-based FT catalysts has only been reported a few times in the open literature. For instance, some papers deal with its potential to shift the product distribution in the FT reaction by increasing the olefin selectivity and decreasing the undesired $CH_4$ production.[13,14] Other works have reported that MnO acts as a CO shift converter promoter and thus to catalyze the water-gas shift reaction (i.e., the transformation from $CO + H_2O$ to $H_2 + CO_2$).[15,16] The occurrence of this reaction can influence the reaction kinetics in the FT reaction and may be interesting when a rich CO syngas composition is used (e.g., the syngas obtained from high temperature coal gasification).[17] The use of manganese for Co-based FT catalysts can also be found in the patent literature.[18] However, the exact role of manganese and its influence on the cobalt active site composition remain largely unclear.

To get a better understanding of the physicochemical and catalytic properties of Co/Mn/$TiO_2$ catalysts, and more specifically the role played by manganese a full in situ characterization of the oxidation state and the local order around the active species of these materials in the calcined state and the reduced state is required. X-ray absorption spectroscopy (XAS) provides insight into the electronic structure and the local order around a selected type of atom and is a particularly well-suited method for the study of the active phase of bimetallic catalysts. Indeed, XAS that does not rely on long-range order allows for an extensive characterization of the geometrical structures and bond distances in materials that lack detectable long range. Another advantage of this technique is that it is element specific and thus can allow for the local order around Co and Mn to be investigated independently. For these reasons, these techniques have already been extensively applied to characterize several types of FT catalyst systems with various promoting transition metals such as Re, Ru, and Pt and various supports such as $Al_2O_3$, $SiO_2$, $NbO_x$, and $TiO_2$ and important information such as the metal oxidation states, the metal nanocrystallite sizes, and the role of the promoter could be successfully unraveled.

In this work, we present a detailed characterization study of a series of Mn-promoted Co/$TiO_2$ FT catalysts, synthesized by various methods with the aim of obtaining different manganese locations at the catalyst surface. This has certainly provided a broader perspective on the role of manganese on the chemical state of cobalt. The influence of the synthesis method and the use of Mn as a promoter on the physicochemical state and reducibility of the cobalt particles have been evaluated using a variety of characterization techniques, namely, X-ray diffraction (XRD), temperature-programmed reduction (TPR), X-ray absorption fine structure (XAFS) spectroscopy, and transmission electron microscopy (TEM). In addition, the $Co^0$ particle sizes and cobalt reduction extents achieved after reduction have been correlated with the FT catalytic results in order to establish structure−performance relationships.

**TABLE 1: Overview of the Catalysts Prepared with the Corresponding Sample Code, the Metal Loadings, and the XRD Visible Crystalline Phase as Well as the Mean Size of the Supported Crystallites**

| sample code | preparation method | wt % Co[a] | wt % MnO[a] | XRD phase and mean size |
|---|---|---|---|---|
| I−Co | IWI Co | 11.1 | | 35 nm $Co_3O_4$ |
| I−CoMn | IWI Co + IWI Mn | 11.0 | 1.4 | 33 nm $Co_3O_4$ |
| I−MnCo | IWI Mn + IWI Co | 9.5 | 1.3 | 18 nm $Co_3O_4$ |
| H−Co | HDP Co | 8.0 | | 15 nm $Co_3O_4$ |
| H−CoMn | HDP Co + IWI Mn | 7.8 | 2.6 | 13 nm $Co_3O_4$ |
| Hcop−CoMn | HDP (Co + Mn) | 7.7 | 7.0 | 17 nm $Co_{2.1}Mn_{0.9}O_4$ |

[a] As calculated by XRF.

## Experimental Section

**1. Catalyst Preparation.** Two groups of $TiO_2$-supported catalysts were synthesized using, respectively, the homogeneous deposition precipitation (HDP) and the incipient wetness impregnation (IWI) methods. The syntheses were performed using aqueous precursor solutions of $Co(NO_3)_2 \cdot 6H_2O$ (Acros Organics, p.a.) and $Mn(NO_3)_2 \cdot 4H_2O$ (Merck, p.a.) and Degussa P25 $TiO_2$ (surface area of 45 $m^2/g$ and pore volume of 0.27 $cm^3/g$) as the support material. In the HDP synthesis, $TiO_2$ powder was suspended in aqueous solutions containing the metal nitrates and the pH was increased by urea decomposition at 90 °C for 18 h under continuous stirring. The materials were subsequently washed in demineralized water, dried at 110 °C in air, and sieved to 0.22−0.5 mm before the following preparation step. For the IWI method, a presieved $TiO_2$ material (0.22−0.5 mm) was used. In all cases, calcinations were carried out in a flow of air at 400 °C for 4 h (ramp 5 °C/min).

A first Co/$TiO_2$ catalyst coded H−Co was prepared in one HDP step to load the cobalt followed by calcination. A portion of the previous dried Co/$TiO_2$ precursor was loaded with manganese in a second IWI step and calcined to give the H−CoMn catalyst. A third catalyst was prepared from a mixture of Co and Mn nitrate solutions in a single HDP step followed by calcination to obtain the catalyst coded Hcop−CoMn. Using the IWI method, a first Co/$TiO_2$ catalyst coded I−Co was prepared in a IWI step followed by drying and calcination. A portion of this oxidized Co/$TiO_2$ precursor was subsequently loaded with manganese and calcined again, leading to the catalyst coded I−CoMn. A last catalyst coded I−MnCo was prepared following the same procedure as the previous catalyst but inverting the order of impregnation. All of the prepared catalysts together with their sample codes, preparation method, and metal loadings are summarized in Table 1.

**2. Catalyst Characterization.** The cobalt and manganese loadings of all calcined samples were determined by X-ray fluorescence (XRF) analysis using a Spectro X-lab 2000 spectrometer. From these results, the total weight % of Co and MnO in all of the catalysts was calculated.

The oxidized catalysts were analyzed by powder X-ray diffraction (XRD) using an ENRAF-NONIUS XRD system equipped with a curved position-sensitive INEL detector and applying a Co $K\alpha_1$ radiation source ($\lambda = 1.788\ 97$ Å). The mean $Co_3O_4$ crystallite sizes were determined using the line broaden-

ing of the reflections localized at 42.9, 70.1, and 77.4°, applying the Scherrer equation (Table 1).

X-ray absorption fine structure (XAFS) spectroscopy at the Co and Mn K-edges was used to investigate the local environment and electronic properties of the Co and Mn atoms in the catalysts before, during, and after reduction treatments. The XAFS measurements were carried out in situ under a dynamic atmosphere in an in-house reactor cell operating at 1 bar.[19] Appropriate amounts of a specific sample were finely crushed and pressed at 2 bar into 0.7 $cm^2$ pellets. All of the samples were measured in a He flow at room temperature (RT) before reduction. Consecutively, the temperature was raised with a ramp of 5 °C/h to the reduction temperature and held until the end of the measurements. The catalysts were reduced at 300 and 350 °C for 2 h with 100 mL/min of 50% $H_2$/He flow. After 2 h of reduction, the catalysts were measured under the final reduction conditions.

Extended X-ray absorption fine structure (EXAFS) spectra were measured at the beginning and at the end of each reduction treatment, while X-ray absorption near-edge (XANES) spectra were recorded continuously throughout the reduction. XAFS data were collected on the DUBBLE beamline (BM26A) at the European Synchrotron Radiation Facility (ESRF, Grenoble, France), operating under beam conditions of 6 GeV, 200 mA, and $2 \times {}^1/_3$ filling mode and using a Si(111) double-crystal monochromator. XAFS signals were measured in fluorescence mode at the Co K-edge (7716 eV) and Mn K-edge (6539 eV). $Co_3O_4$, $MnO_2$, $Mn_2O_3$, and MnO powders (Aldrich, 99.999%) were used as reference materials.

Data reduction of the experimental X-ray absorption spectra was performed with the program EXBROOK.[20] A pre-edge background subtraction and normalization was carried out by fitting a linear polynomial to the pre-edge region and a cubic spline at the post-edge region of the absorption spectrum. A smooth atomic background was then obtained. EXAFS refinements were performed with the EXCURV98 package.[20] Phase shifts and backscattering factors were calculated ab initio using Hedin−Lundqvist potentials. Refinements were carried out using $k^1$ and $k^3$ weighting in the ranges 3.5−12 and 3.5−9 $Å^{-1}$ for the Co and Mn K-edges, respectively. The effects of anharmonicity due to the presence of very small Co metallic particles were corrected with the cumulant expansion feature implemented in EXCURV98 using the coefficient of linear expansion of cobalt metal ($14.6 \times 10^{-6}$ m/°C) at the Co K-edge. The AFAC parameters (amplitude reduction factor) calibrated from the fit of the Co and Mn metal foils were respectively fixed at 0.65 and 0.80 for the Co and Mn K-edges, respectively.

In the reduced catalysts, the general morphology of the material, the Co particle distributions, as well as the average Co particle sizes were investigated by transmission electron microscopy (TEM) using a Tecnai 20 FEG TEM microscope operating at 200 kV equipped with an energy-dispersive X-ray (EDX) analyzer. The calcined catalysts were initially dried in a flow of air at 120 °C for 30 min. Subsequently, the flows were adjusted to 50% $H_2$/He and the temperature was raised to 350 °C at a rate of 5 °C/min. After 2 h of reduction at 350 °C, the temperature was decreased to 150 °C and a passivation was carried out in a 5% $CO_2$/He flow for 30 min. Reduced/passivated samples were ground and ultrasonically dispersed in ethanol. A drop of suspension was then air-dried on a holey carbon film, and bright field micrographs were collected. The average diameter of the Co particles was estimated by measuring 200−300 single particles contained in 5−10 TEM images for each of the catalysts and applying the following formula: average Co size (nm) $= \sum n^3/\sum n^2$, with $n$ being the diameter of each measured Co particle in nanometers.

The bulk reducibility of the catalysts was investigated by temperature-programmed reduction (TPR) using a Thermo electron TPDRO 1100 instrument. The calcined materials were loaded in a tubular quartz reactor and flushed with Ar at 120 °C for 1 h. Subsequently, the reactor was cooled to RT and the gas flow was adjusted to 5% $H_2$/Ar. The temperature was then raised from RT to 700 °C at a rate of 10 °C/min, and the content of $H_2$ in the gas outlet was monitored with a thermoconductivity detector throughout the reduction.

The spatial distribution of Co, Mn, and Ti atoms in the Hcop−CoMn reduced/passivated catalyst was investigated by scanning transmission electron microscopy with electron energy loss spectroscopy (STEM-EELS). The Ti, Mn, and Co $L_{2,3}$-edges and the O K-edge were monitored by using a 100 keV STEM instrument (VG HB 501) equipped with a field emission source and a parallel Gatan 666 EELS spectrometer. The instrument was in operation in Orsay and produced EELS spectra with a 0.5 eV energy resolution and sub-nanometer spatial resolution within a typical acquisition time of less than 1 s per pixel, as described in more detail by Stephan et al.[21] The sample was first sonicated in ethanol and then dropped on a holey carbon film supported on a copper grid.

**3. Catalyst Testing.** The behavior of the catalysts in the Fischer−Tropsch reaction was investigated under isothermal plug-flow conditions. Typically, the oxidized catalyst particles (0.2−0.5 mm) were diluted at 20% in SiC particles (0.1−0.3 mm) and loaded into a glass reactor (5 cm diameter). The samples were activated at a 20 mL/min flow of $H_2$ at 300 and 350 °C for 2 h and subsequently cooled to 220 °C at a rate of 10 °C/min in a He flow. The conditions were then adjusted for the FT reaction at 1 bar, 220 °C, and a syngas flow of 12 mL/min ($H_2$/CO ratio of 2). Gas hourly space velocities of 3010 $h^{-1}$ were used in all experiments, leading to CO conversions in the range 2−6%. The hydrocarbon product composition was analyzed on-line every 60 min and monitored during the first 60 h of reaction using a Varian CP-3800 gas chromatograph equipped with a fused silica column of 50 m length and a flame ionization detector (FID). The catalytic performances were evaluated after 60 h of reaction by comparing Co time yields ($10^{-5}$ mol of CO (g Co)$^{-1}$ $s^{-1}$), turnover frequencies (TOF $= 10^{-3}$ $s^{-1}$), and selectivity expressed in percentages of CO converted to $CH_4$ and $C_{5+}$ fraction of products.

## Results and Discussion

**1. Characterization of the Catalysts in the Calcined State.** *1.1. X-ray Diffraction.* The XRD patterns of the oxidized catalysts are shown in Figure 1. In addition to the reflections originating from the anatase and rutile $TiO_2$ phases, the diffraction peaks corresponding to a spinel $Co_3O_4$ phase are detected at $2\theta = 36.4$, 42.9, 52.3, 70.1, and 77.4°, indicating the formation of $Co_3O_4$ crystallites in all catalysts. These reflections are much weaker in H−Co and H−CoMn, suggesting a less crystalline character of the $Co_3O_4$ phase and/or the presence of some amorphous Co phase in these catalysts. In the Hcop−CoMn catalyst, the positions of these reflections are slightly shifted toward smaller $2\theta$ angles, indicating an enlargement of the $Co_3O_4$ unit cell. As will be discussed later, this increase of the cell parameter is due to the incorporation of $Mn^{3+}$ ions into the $Co_3O_4$ structure leading to the formation of $Co_{3-x}Mn_xO_4$ solid solutions. An estimation of the average stoichiometry of the Hcop−CoMn catalyst corresponding to the reflections shift using the Vegard plot reported for the

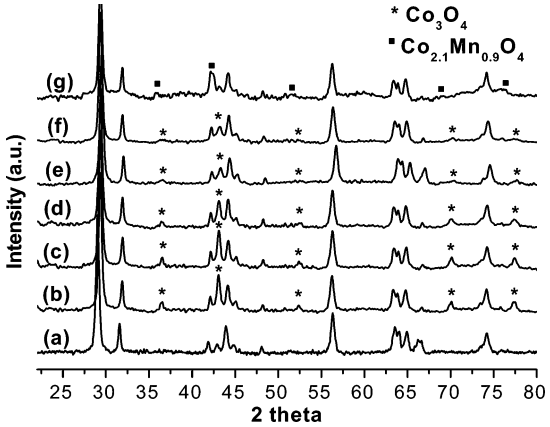


**Figure 1.** XRD patterns of $TiO_2$ P25 (a) and the I−Co (b), I−CoMn (c), I−MnCo (d), H−Co (e), H−CoMn (f), and Hcop−CoMn (g) catalysts after calcination.

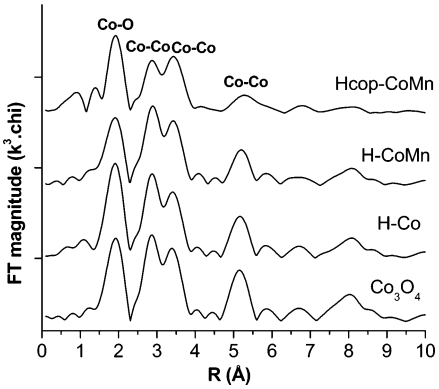


**Figure 2.** $k^3$-weighted Fourier transforms of the experimental EXAFS spectra at the Co K-edge for $Co_3O_4$ (a) and the H−Co (b), H−CoMn (c), and Hcop−CoMn (d) catalysts after calcination.

$Co_{3-x}Mn_xO_4$ solid solutions[22] gave $Co_{2.1}Mn_{0.9}O_4$. The mean $Co_3O_4$ particle sizes resultant from XRD calculations were somewhat smaller in the catalysts prepared by HDP (∼13−17 nm) than in the IWI catalysts (∼31−33 nm), with the exception of the I−MnCo catalyst, in which values of 18 nm were obtained (Table 1).

*1.2. X-ray Absorption Spectroscopy.* 1.2.1. Co K-Edge. Table 2 summarizes the results of the EXAFS refinements for the first three coordination shells (Co−O and Co−Co). Except H−CoMn and Hcop−CoMn, which show slightly longer bond distances, all of the catalysts present similar results. The first oxygen shell coordination number ranges from 4.2 in Hcop−CoMn to 5.5 in I−Co, whereas all of the samples exhibit the same Co−O distance of 1.91 Å, except the H−CoMn and Hcop−CoMn catalysts which feature slightly longer bond distances of 1.92 and 1.93 Å, respectively. The second and third Co shells are also very similar in all of the catalysts with 3.3−4.4 Co atoms at 2.85 Å and 7−10 Co atoms at 3.36 Å. Once again, H−CoMn and Hcop−CoMn present longer distances of 2.86 and 2.87 Å for the first Co shell and 3.38 and 3.40 Å for the second Co shell, respectively. In agreement with the XRD results, the EXAFS results indicate that in all catalysts except H−CoMn and Hcop−CoMn cobalt belongs almost entirely to a $Co_3O_4$ phase. Additionally, a minor amount of cobalt may also be present as cobalt titanate species (e.g., $CoTiO_3$), which are likely formed upon calcination treatments at high temperatures.[23] Nonetheless, the presence of these compounds cannot be detected by XAFS, since this technique only measures the average environment of the Co atoms and these have been shown to exist mostly as large $Co_3O_4$ clusters.

Indeed, the Co environment obtained with EXAFS corresponds to a spinel arrangement of atoms in $Co_3O_4$ with $Co^{2+}$ and $Co^{3+}$ ions located, respectively, in $T_d$ and $O_h$ coordination,[24,25] giving an average environment around the Co atoms of 5.3 O at 1.91 Å and 4 and 8 Co at 2.85 and 3.36 Å. The longer interatomic distances found for H−CoMn and Hcop−CoMn combined with the slight shift of the $Co_3O_4$ reflections in the XRD patterns are certainly pointing toward the formation of $Co_{3-x}Mn_xO_4$-type solid solutions by substitution of $Co^{3+}$ by $Mn^{3+}$ in the $Co_3O_4$ structure. These solid solutions can indeed be prepared in a broad range of compositions and readily form under conditions of high temperature and oxygen environment.[26,27] Due to the greater atomic radius of $Mn^{3+}$ (1.37 Å) with respect to $Co^{3+}$ (1.25 Å),[28] substitution of $Co^{3+}$ by $Mn^{3+}$ in the $O_h$ sites results in a cell expansion, increasing steadily with increasing Mn content in the $Co_3O_4$ structure.[22,29,30] This phenomenon is also reflected in the Fourier transforms for the HDP catalysts, as illustrated in Figure 2, which shows a decrease of the fourth Co−Co shell intensity as the Mn loading increases. This indicates the presence of a higher level of disorder in the structure of these catalysts that is very likely induced by the incorporation of $Mn^{3+}$ ions into the $Co_3O_4$ lattice. Furthermore, this effect is more pronounced in Hcop−CoMn, since a higher amount of Mn is mixed with the $Co_3O_4$ phase.

1.2.2. Mn K-Edge. The oxidation state of manganese was investigated in the first derivative of the XANES spectra, which were compared with those of suitable reference materials.[31]

**TABLE 2: Results of the EXAFS Analysis at the Co and Mn K-Edges for the Calcined Co/$TiO_2$ and Co/Mn/$TiO_2$ Catalysts and for $Co_3O_4$ and $MnO_2$ Reference Materials (n.a. = Not Applicable)**

| sample | *R* (Å) Co−O | N atoms | $2\sigma^2$ (Å) | *R* (Å) Co−Co | N atoms | $2\sigma^2$ (Å) | *R* (Å) Mn−O | N atoms | $2\sigma^2$ (Å) | *R* (Å) Mn−Mn | N atoms | $2\sigma^2$ (Å) |
|---|---|---|---|---|---|---|---|---|---|---|---|---|
| $Co_3O_4$ | 1.92 | 5.3 O | 0.005 | 2.85 | 4.0 Co | 0.005 | n.a. | n.a. | n.a. | n.a. | n.a. | n.a. |
| | | | | 3.36 | 8.0 Co | 0.008 | | | | | | |
| I−Co | 1.91 | 5.5 O | 0.009 | 2.84 | 3.9 Co | 0.005 | n.a. | n.a. | n.a. | n.a. | n.a. | n.a. |
| | | | | 3.35 | 8.0 Co | 0.012 | | | | | | |
| I−CoMn | 1.91 | 4.7 O | 0.003 | 2.85 | 3.5 Co | 0.006 | 1.88 | 5.7 O | 0.002 | 2.87 | 2.5 Mn | 0.001 |
| | | | | 3.35 | 7.0 Co | 0.011 | | | | 3.43 | 2.6 Mn | 0.003 |
| I−MnCo | 1.91 | 5.2 O | 0.003 | 2.85 | 3.8 Co | 0.005 | 1.88 | 6.0 O | 0.011 | 2.87 | 2.2 Mn | 0.001 |
| | | | | 3.36 | 7.3 Co | 0.010 | | | | 3.45 | 3.6 Mn | 0.030 |
| H−Co | 1.91 | 5.4 O | 0.004 | 2.85 3.36 | 3.3 Co 8.3 Co | 0.003 0.013 | n.a. | n.a. | n.a. | n.a. | n.a. | n.a. |
| H−CoMn | 1.92 | 5.1 O | 0.004 | 2.86 | 5.2 Co | 0.009 | 1.91 | 5.7 O | 0.007 | 2.87 | 4.2 Mn | 0.010 |
| | | | | 3.38 | 6.9 Co | 0.012 | | | | 3.39 | 1.8 Mn | 0.009 |
| Hcop−CoMn | 1.93 | 4.2 O | 0.003 | 2.87 | 4.1 Co | 0.013 | 1.91 | 4.2 O | 0.007 | 2.89 | 4.7 Mn | 0.013 |
| | | | | 3.40 | 9.9 Co | 0.018 | | | | 3.43 | 12.4 Mn | 0.034 |
| | | | | | | | | | | 3.73 | 8.8 Mn | 0.023 |
| $MnO_2$ | n.a. | n.a. | n.a. | n.a. | n.a. | n.a. | 1.88 | 6.0 O | | 2.88 | 4.2 Mn | |
| | | | | | | | | | | 3.38 | 6.4 Mn | |

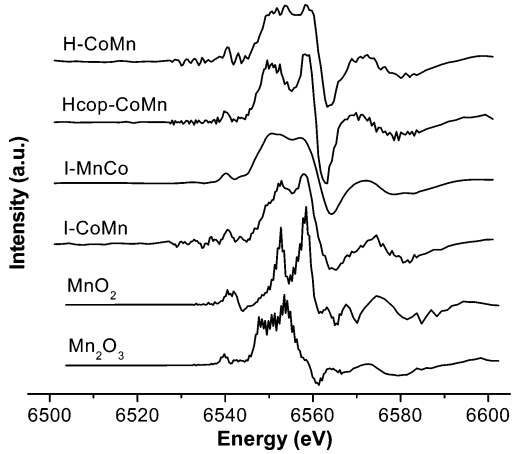


**Figure 3.** First derivative of the XANES spectra of the I−CoMn, I−MnCo, H−Co, and Hcop−CoMn catalysts after calcination and of the $MnO_2$ and $Mn_2O_3$ reference materials.

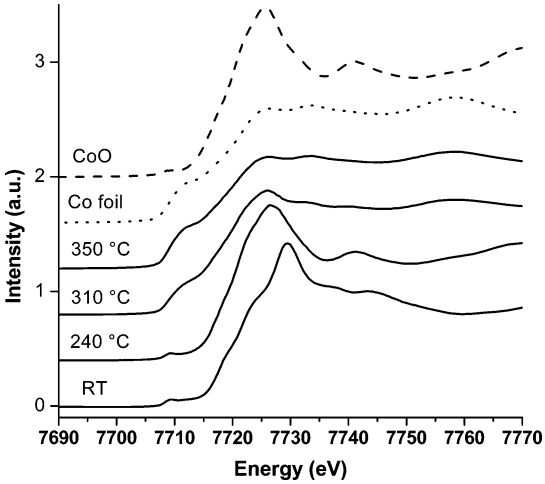


**Figure 4.** Normalized XANES spectra at the Co K-edge of the I−Co catalyst measured at different temperatures during the reduction. For reference proposes, it also includes the spectra of metallic Co and CoO.

Spectra for the oxidized catalysts and for the $MnO_2$ and $Mn_2O_3$ materials are displayed in Figure 3. All catalysts contain a main component of $Mn^{4+}$, as deduced from the peak at 6559 eV also present for $MnO_2$. The high similarity between the spectra for $MnO_2$ and I−CoMn suggests that this catalyst contains mainly $Mn^{4+}$ species, most probably in the form of $MnO_2$. In the other catalysts, a $Mn^{3+}$ component is also detected in the spectra, as indicated by the peak at 6550 eV corresponding to $Mn_2O_3$. Therefore, these results show that in all catalysts after calcination the manganese exists mainly in a $Mn^{4+}$ state and with some admixture of $Mn^{3+}$, which is present in larger amounts in H−CoMn and Hcop−CoMn. Additionally, a small $Mn^{3+}$ component is also detected for the I−MnCo sample, suggesting that $Mn^{3+}$ species may also exist dispersed at the $TiO_2$ surface. This is also suggested by the little structure observed in the spectrum, being indicative of a low range ordered manganese structure.

The results of the EXAFS refinement for the catalysts and for the α-$MnO_2$ material are summarized in Table 2. All of the catalysts except H−CoMn and Hcop−CoMn present the same interatomic distances with a first shell of 5.7−6 O at 1.88 Å and second and third Mn−Mn shells at distances of ∼2.88 and ∼3.38−3.45 Å, respectively. H−CoMn and Hcop−CoMn feature a slightly larger Mn−O bond distance of 1.91 Å, similar to the results obtained at the Co K-edge. In Hcop−CoMn, however, the O coordination of 4.2 shows a marked drop compared to all other catalysts. Therefore, in agreement with the XANES analysis, EXAFS confirms that most of the Mn atoms in I−CoMn and I−MnCo belong to a α-$MnO_2$-type phase. However, this manganese phase is amorphous and/or possesses a strong nanocrystalline character, since the XRD patterns did not show any corresponding visible reflections. This is also confirmed by the relatively flat shape of the XANES derivative indicative of a highly dispersed phase, as well as by the very low intensity of the second and third peaks in the Fourier transforms (not shown).[32] In contrast, the clearly longer Mn−O bond distances of 1.91 Å found in the HDP catalysts strongly suggest the presence of other phases in addition to α-$MnO_2$. Indeed, EXAFS at both the Co and Mn K-edges reveals for H−CoMn and Hcop−CoMn a marked elongation of the bond distances around both Co and Mn atoms. These results combined with the XRD results clearly point toward the formation of solid solutions of the spinel type $Co_{3-x}Mn_xO_4$ in both catalysts.

While the increase in the Co−O bond distance correlates directly to the increase of the cell volume upon manganese incorporation, the increase of the Mn−O bond distance on the other hand correlates to the fraction of Mn atoms incorporated in these solid solutions. Thus, the Mn−O distances measured in the HDP catalysts are an average between those of $MnO_2$ (1.88 Å) and those of $Co_{3-x}Mn_xO_4$ (1.92−1.96 Å).[30] Hence, the formation of $Co_{3-x}Mn_xO_4$ solid solutions occurs not only in Hcop−CoMn but also in H−CoMn, as revealed by EXAFS giving in both catalysts Mn−O distances of 1.91 Å. Taking into account the higher Mn loading contained in Hcop−CoMn compared to H−CoMn and, in turn, the same Mn−O distances measured with EXAFS (1.91 Å), this catalyst is expected to contain also a fair fraction of manganese in the form of $MnO_2$.

**2. Redox Behavior of Calcined Catalysts.** The change in cobalt oxidation state occurring throughout reduction of the catalysts has been monitored by XANES at the Co K-edge. XANES spectra collected continuously during the temperature increase have been used as fingerprints to identify the cobalt oxidation state at the different stages of reduction. As an example, Figure 4 shows the XANES spectra collected at RT, 240, 310, and 350 °C during reduction of the I−Co catalyst. The figure also includes the spectra of Co foil and CoO for comparison. Dramatic changes both in terms of white line intensity, oscillation shape, and edge position are occurring as a function of the temperature. Observation of the shape of the spectra suggests that the reduction of $Co_3O_4$ into Co metal takes place in several steps with a marked intermediate stage at 240 °C. Detailed comparison of the spectrum measured at 240 °C with that of CoO that features the same shape and edge position (7721 eV) shows that this intermediate stage corresponds to a CoO phase. CoO is then fully reduced into $Co^0$ in a second stage at ∼350 °C, as indicated by the large decrease in intensity of the white line in the spectra. The reduction behavior was found to be similar in all of the catalysts investigated, although a full reduction from CoO to $Co^0$ metal was not always achieved as a result of using the HDP preparation method or manganese as a promoter.

Figure 5 presents the TPR profiles of the six catalysts, illustrating the cobalt reducibility as a function of the preparation method and chemical composition. Due to the presence of manganese in the catalysts, the reduction profiles may contain variable contributions from different compounds, and for this reason, quantification of the areas was not taken into account. Hence, the data were merely used to evaluate the cobalt reducibility in the different catalysts, while quantifications were further carried out by XANES analysis.[31] Figure 5 shows two main peaks in all reduction profiles, which are ascribed to the reduction steps

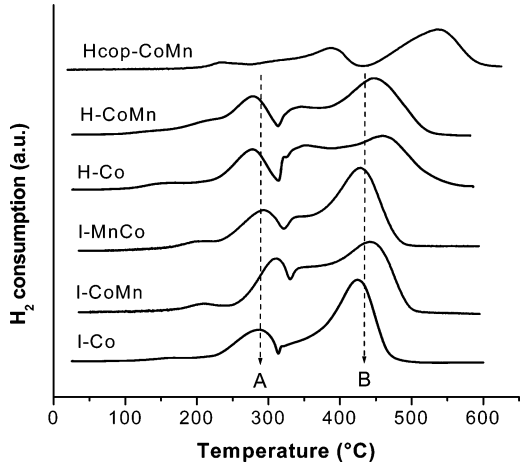


**Figure 5.** Temperature-programmed reduction profiles for the I−Co, I−CoMn, I−MnCo, H−Co, H−CoMn, and Hcop−CoMn catalysts.

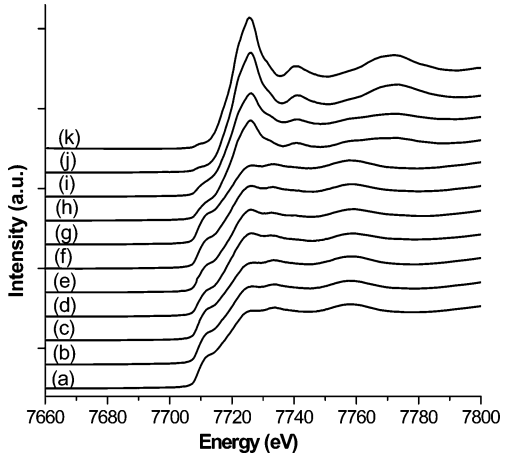


**Figure 6.** Normalized XANES spectra at the Co K-edge of the I−Co (a), I−CoMn (b), I−MnCo (c), H−Co (d), H−CoMn (e), and Hcop−CoMn (k) catalysts after 2 h reduction at 350 °C; and of the I−Co (f), I−CoMn (g), I−MnCo (h), H−Co (i), and H−CoMn (j) after 2 h reduction at 300 °C.

from $Co_3O_4$ to CoO and from CoO to metallic cobalt. In the IWI catalysts, both reduction steps take place at around 280 and 425 °C and are not largely influenced by the presence of manganese. Nevertheless, for the I−CoMn catalysts, both peak maxima are shifted to 305 and 450 °C, suggesting a slight decrease of the cobalt reducibility. The TPR profiles for the H−Co and H−CoMn catalysts also exhibit typical reduction steps, although the second step is broader and contains two peak maxima at ∼350 and ∼465 °C, most likely due to a different interaction of the cobalt particles with the $TiO_2$. Moreover, the peak at 465 °C is somewhat more pronounced for H−CoMn than for H−Co, again suggesting lower cobalt reducibility caused by manganese. Thus, the HDP catalysts display lower cobalt reducibility than the IWI catalysts, probably due to the presence of smaller cobalt oxide particles. A very different TPR profile was obtained for Hcop−CoMn, showing the $H_2$-consumption peaks at 370 and 550 °C. This clearly indicates a much lower cobalt reducibility compared to all other catalysts. This effect is caused by manganese incorporated in the $Co_3O_4$ structure and is in agreement with other work in which TPR experiments with mixed Co−Mn spinels led to similar reduction profiles.[33]

As a consequence of this multistage process, reduction of the catalysts led to different cobalt reduction degrees largely influenced by the properties of the catalyst precursors. The XANES spectra obtained for all catalysts after 2 h of reduction at 300 and 350 °C are shown in Figure 6. Cobalt oxide is fully reduced to Co metal at 350 °C in I−Co, I−CoMn, and I−MnCo catalysts, as observed by the XANES spectral shape and the edge position featuring a $Co^0$ oxidation state. H−Co and H−CoMn catalysts reduced at 350 °C, however, still contain also a small fraction of $Co^{2+}$, as evidenced by a weak white line present at 7725 eV. Finally, the spectrum of Hcop−CoMn reduced at 350 °C corresponds to a pure $Co^{2+}$ state. Hence, in agreement with the TPR results, the Hcop−CoMn catalyst is by far the most resistant against reduction, as it contains a $Co_{3-x}Mn_xO_4$ phase with low cobalt reducibility. On the other hand, reduction at 300 °C led to various mixtures of $Co^0$ and CoO in the catalysts. Reduction extents were quantified by means of a linear combination of the XANES spectra of pure CoO and $Co^0$ references, and the percentages of $Co^0$ for each catalyst are summarized in Table 3. All IWI catalysts resulted in 100% of $Co^0$ with the exception of I−CoMn reduced at 300 °C, for which 48% $Co^0$ was found. Lower reduction degrees were obtained for H−Co and H−CoMn with values of 95 and 90% $Co^0$ at 350 °C and 40 and below 5% at 300 °C, respectively.

**TABLE 3: EXAFS Results at the Co K-Edge for the Co/$TiO_2$ and Co/Mn/$TiO_2$ Catalysts in Situ Reduced in $H_2$/He Flow at 300 and 350 °C for 2 h (The Data for a Co Metal and CoO Materials Are Included for Comparison; n.a. = Not Applicable)**

| sample code | reduction temp (°C) | % $Co^0$ | N atoms[a] ($Co^0$ phase) | $R$ (Å) distance | $2\sigma^2$ (Å) | N atoms (CoO phase) | $R$ (Å) distance | $2\sigma^2$ (Å) |
|---|---|---|---|---|---|---|---|---|
| Co metal | n.a. | 100 | 12 Co | 2.51 | n.a. | n.a. | n.a. | n.a. |
| CoO | n.a. | 0 | n.a. | n.a. | n.a. | 6.0 O | 2.13 | n.a. |
| | | | | | | 12 Co | 3.02 | |
| I−Co | 300 | 92 | 9.4 Co | 2.51 | 0.020 | n.a. | n.a. | n.a. |
| | 350 | 100 | 9.3 Co | 2.51 | 0.022 | n.a. | n.a. | n.a. |
| I−CoMn | 300 | 48 | 6.8 Co | 2.50 | 0.023 | 4.7 O | 2.13 | 0.033 |
| | | | | | | 9.9 Co | 3.04 | 0.036 |
| | 350 | 100 | 10.2 Co | 2.52 | 0.027 | n.a. | n.a. | n.a. |
| I−MnCo | 300 | 97 | 11.2 Co | 2.53 | 0.029 | n.a. | n.a. | n.a. |
| | 350 | 100 | 9.6 Co | 2.52 | 0.021 | n.a. | n.a. | n.a. |
| H−Co | 300 | 40 | 2.3 Co | 2.49 | 0.008 | 3.9 O | 2.12 | 0.042 |
| | | | | | | 10.2 Co | 3.02 | 0.032 |
| | 350 | 95 | 9.4 Co | 2.52 | 0.023 | n.a. | n.a. | n.a. |
| H−CoMn | 300 | >5 | 1.7 Co | 2.527 | 0.014 | 3.8 O | 2.22 | 0.023 |
| | | | | | | 10.2 Co | 3.09 | 0.026 |
| | 350 | 90 | 11.4 Co | 2.52 | 0.027 | n.a. | n.a. | n.a. |
| Hcop−CoMn | 350 | <5 | 1.0 Co | 2.485 | 0.014 | 3.8 O | 2.18 | 0.028 |
| | | | | | | 15.0 Co | 3.11 | 0.033 |

[a] Extent of Co reduction calculated by a linear combination of the XANES spectra of pure Co metal and CoO.

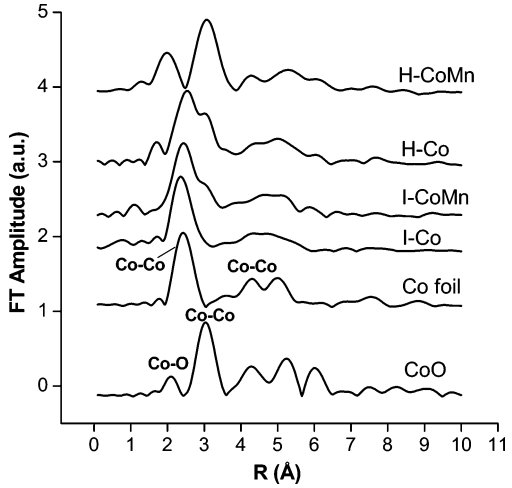


**Figure 7.** $k^3$-weighted Fourier transforms of the experimental EXAFS spectra at the Co K-edge for CoO and Co foil and for the I−Co, H−CoMn, and Hcop−CoMn catalysts after reduction at 300 °C.

On the basis of these results, it is concluded that manganese hampers the cobalt bulk reducibility, with this effect being further accentuated by the existence of Co−Mn interactions, as in the case of the Hcop−CoMn and H−CoMn catalysts. Furthermore, the HDP catalysts generally led to lower cobalt reducibility, probably due to a stronger Co−support interaction.[34]

**3. Physicochemical Characterization of Reduced Catalysts.** *3.1. EXAFS at the Co K-Edge.* To gain insight into the local environment and electronic structure of the Co atoms in the reduced catalysts, EXAFS spectra at the Co K-edge were collected. Measurements after in situ reduction treatments at 300 and 350 °C show spectra characteristic of either Co metal, CoO, or mixtures of both compounds. This can be observed at first glance in the Fourier transforms (Figure 7), showing different shapes for each catalyst, with peaks corresponding to a combination of Co metal and CoO materials, which are also presented in Figure 7. Indeed, the Fourier transforms reflect different Co reduction extents with the shells of Co metal dominating in the highly reduced catalysts, for example, I−Co reduced at 300 °C, while the two Co−O and Co−Co shells of CoO increase in intensity with lower cobalt reduction extents.

The EXAFS results summarized in Table 3 confirm the preliminary observation, since all reduced catalysts could be fitted with a combination of the structural parameters of Co metal and CoO. As a result, the structure of all reduced catalysts consists of various shells with similar interatomic distances to those found in $Co^0$ and CoO materials, and with coordination numbers closely related to the relative fractions of CoO and $Co^0$ present in the catalysts. All catalysts feature a Co−Co shell with distances of around 2.51−2.53 Å and with coordination numbers ranging from 1.0 to 11.2. This shell belongs to the metallic phase with either face-centered cubic (fcc) or hexagonal close-packed (hcp) structure that features on average a first shell of 12 Co atoms at 2.52 Å. This was determined by the EXAFS fit of the Co foil and is in agreement with the crystallographic data.[24] Therefore, the low Co−Co coordination numbers in the catalysts reflect the occurrence of numerous surface atoms that characterize nanosized $Co^0$ particles as well as the presence of a Co oxidic phase next to the Co metal phase in the incompletely reduced catalysts. In fact, the number of Co neighboring atoms forming this shell drastically decreases as a function of the reduction degree and/or the $Co^0$ particle size. For instance, the I−Co catalyst reduced at 350 °C gives 10.3 Co neighbor atoms in contrast to the reference $Co^0$ material with 12. I−CoMn reduced at 300 °C gives 6.8 Co neighbor atoms due to the low reduction degree (48%).

**TABLE 4: Results of the EXAFS Analysis at the Mn K-Edge for the Catalysts Reduced at 300 and 350 °C and for MnO and $Ti_2MnO_4$ Reference Materials (n.a. = Not Applicable)**

| sample | red. temp (°C) | $R$ (Å) Mn−O | N atoms | $2\sigma^2$ (Å) | $R$ (Å) Mn−Mn | N atoms | $2\sigma^2$ (Å) |
|---|---|---|---|---|---|---|---|
| MnO | n.a. | 2.20 | 6 O | n.a. | 3.14 | 12 Mn | n.a. |
| $Ti_2MnO_4$ | n.a. | 2.02 | 4.0 O | n.a. | 3.72 | 4.0 Mn | n.a. |
| I−CoMn | 300 | 2.09 | 4.8 O | 0.022 | 3.03 | 1.3 Mn | 0.005 |
| | 350 | 2.04 | 4.0 O | 0.022 | 2.91 | 0.4 Mn | 0.001 |
| I−MnCo | 300 | 2.08 | 5.0 O | 0.030 | 3.05 | 1.5 Mn | 0.032 |
| | 350 | 2.06 | 4.4 O | 0.027 | 3.00 | 0.7 Mn | 0.009 |
| H−CoMn | 300 | 2.07 | 5.2 O | 0.007 | 2.98 | 4.3 Mn | 0.026 |
| | 350 | 2.07 | 5.1 O | 0.027 | 3.04 | 2.3 Mn | 0.025 |
| H−CoMncop | 350 | 2.15 | 5.6 O | 0.025 | 3.07 | 11.9 Mn | 0.033 |

Two additional Co−O and Co−Co shells were obtained for the catalysts with low reduction extents. These shells belong to the fraction of unreduced CoO and have coordination numbers between 3.8 and 4.7 and 9.9 and 10.2, respectively. In agreement with crystallographic data, the EXAFS fit of the CoO cubic structure[25] gives Co atoms 6-fold coordinated by oxygen atoms with Co−O and Co−Co distances of 2.13 and 3.02 Å, respectively (Table 3). It is remarkable to notice that the Co−O and Co−Co distances obtained for the H−CoMn and Hcop−CoMn catalysts are significantly longer (2.18−2.20 and 3.09−3.11 Å) than those in the CoO reference material. This elongation indicates the occurrence of a cell expansion of the CoO phase that is very likely due to the formation of $Mn_{1-x}Co_xO$ solid solutions, as will be discussed in detail later with the results at the Mn K-edge. Indeed, due to the greater ionic radius of $Mn^{2+}$ ions compared to $Co^{2+}$, $Mn_{1-x}Co_xO$ compounds feature a larger cell parameter[28] and longer interatomic distances compared to the CoO reference material. Therefore, these results reflect an intimate mixing of MnO with CoO in the HDP catalysts.

As was already pointed out, the Co reduction degree influences the coordination number of the Co−Co shell at 2.51−2.52 Å, decreasing from a maximum of 12 in a fully reduced bulk $Co^0$ material to zero in pure CoO. Thus, for a fully reduced catalyst, the decrease of the number of Co neighboring atoms is due to a geometric artifact caused by the nanosized character of the metallic particles. Although coordination numbers are determined with a relatively low accuracy with EXAFS (10−20%), they can still be used to roughly estimate particle sizes in the catalysts. The accuracy of this technique is nonetheless enhanced in the case of particles smaller than 3−5 nm. Among the catalysts studied, the XANES results revealed that the I−Co, I−CoMn, and I−MnCo catalysts contain 100% $Co^0$ after reduction at 350 °C (Table 3) and, therefore, their coordination numbers may be directly used to calculate the $Co^0$ particle sizes. However, since the reduction degrees in H−Co and H−CoMn respectively were 95 and 90%, the coordination numbers had to be corrected to take into account the CoO fraction. Finally, the low reduction extent of Hcop−CoMn (<5% $Co^0$) did not allow this calculation method to be applied.

The results of the $Co^0$ particle sizes in the catalysts reduced at 350 °C are presented in Table 5. The $Co^0$ particles turned out to be in the range 3−6 nm, with the exception of the H−CoMn catalyst, which likely contains larger particles according to the high coordination number. The existence of such small particles suggests that a redispersion of the cobalt phase occurs during reduction, leading to a dramatic decrease in the particle sizes.

**TABLE 5: Overview of the Cobalt Particle Size Calculation Obtained by EXAFS and TEM Techniques in the Catalyst Reduced at 350 °C (n.a. = Not Applicable)**

| sample code | EXAFS Co size[a] (nm) | TEM Co size[b] (nm) |
|---|---|---|
| I−Co | 2.5 | 4.3 |
| I−CoMn | 3.7 | 4.9 |
| I−MnCo | 2.7 | 4.8 |
| H−Co | 3.2 | 3.5 |
| H−CoMn | >10 | 5.6 |
| Hcop−CoMn | n.a. | 10.5 |

[a] Co particle sizes calculated using the number of Co neighbor atoms given by the Co metal shell and according to the formula size (nm) = ((*m**2) = 1)*2.51, where *m* is the average number of Co shells surrounding each Co atom in a fcc structure. The Co coordination numbers have also been corrected for the extent of Co reduction before the calculation. [b] Average Co size calculated from the formula *N* (nm) = $\sum n^3/\sum n^2$, with *N* being the average Co diameter size and *n* the diameter of each measured Co particle in nanometers.

*3.2. XAFS at the Mn K-Edge.* Figure 8 presents the first derivative of the XANES spectra obtained for all catalysts after reduction at 300 and 350 °C, along with a MnO reference material. It can be observed that all spectra exhibit a maximum of the first derivative at 6547 eV, indicating the existence of a pure $Mn^{2+}$ oxidation state in all reduced catalysts. However, the spectrum of the MnO material contains much more structure while the maximum of its first derivative is divided into two peaks. This difference in general shape of the spectra between the catalysts and bulk MnO clearly points out the amorphous and dispersed character of the manganese phase, which has a 2+ oxidation state but a different local structure.

The local environment around manganese (i.e., number and distances of neighboring atoms) was determined by EXAFS. The Fourier transforms for all of the reduced catalysts are presented in Figure 9. The Mn phases exhibit a very short-range order, since only a main peak at 2.0−2.2 Å corresponding to a Mn−O coordination shell and a very weak second Mn−Mn shell that can be observed at around 3 Å are in most cases very weak. As the XANES analysis already showed, this is a clear indication of a high level of disorder pointing to the existence of highly dispersed manganese species. The exception is the Hcop−CoMn catalyst, which features two intense peaks due the presence of a more bulk-type Mn phase.

The coordination parameters obtained by the *k*-space analysis of the EXAFS data are summarized in Table 4, along with the crystallographic data of MnO and $Ti_2MnO_4$ materials[24] included for comparison. The coordination numbers and interatomic

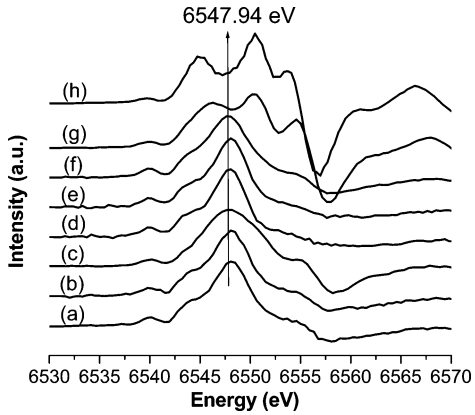


**Figure 8.** First derivative of the normalized XANES at the Mn K-edge for I−CoMn (a), I−MnCo (b), and H−CoMn (c) reduced at 300 °C, I−CoMn (d), I−MnCo (e), H−CoMn (f), and Hcop−CoMn (g) reduced at 350 °C, and a reference MnO material (h).

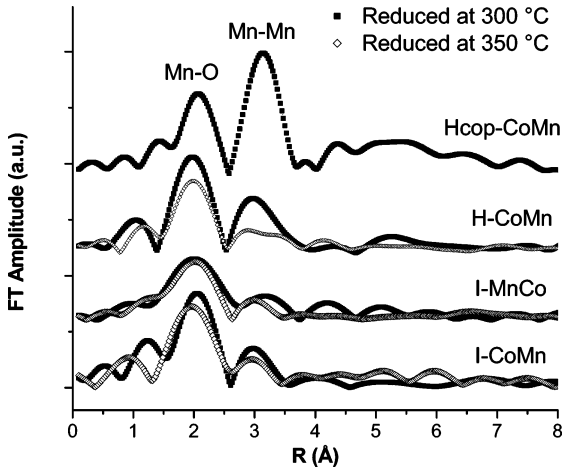


**Figure 9.** $k^3$-weighted Fourier transforms of the experimental EXAFS spectra at the Mn K-edge for the I−CoMn, I−MnCo, H−CoMn, and Hcop−CoMn catalysts after reduction at 350 and 300 °C.

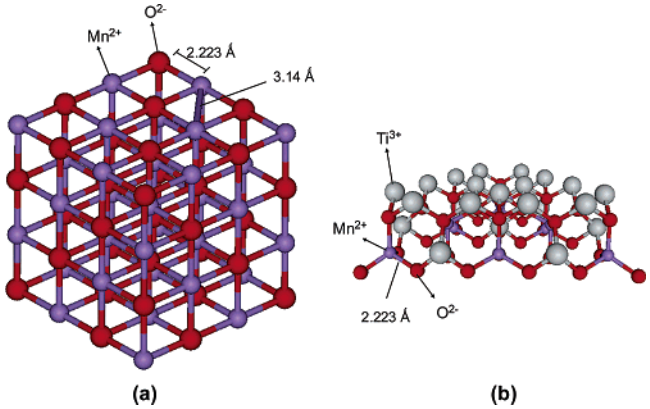


**Figure 10.** Crystallographic structure of MnO with $Mn^{2+}$ in $O_h$ sites (a) and $Ti_2MnO_4$ with $Mn^{2+}$ in $T_d$ sites (b). The figures illustrate several unit cells for both structures including the Mn−O distances.

distances for the Mn−O and Mn−Mn shells vary significantly from one catalyst to another. The coordination numbers of the Mn−O shell range between 5.6 and 4.1, whereas the Mn−O distances vary from 2.15 to 2.04 Å. Comparison of these values with those corresponding to the MnO and $Ti_2MnO_4$ compounds indicates that manganese possesses an average oxygen coordination consisting of a combination of 4-fold and 6-fold coordination, indicating the formation of mixtures of both types of structures. MnO and $Ti_2MnO_4$ compounds contain $Mn^{2+}$ ions, the first in octahedral ($O_h$) and the second in tetrahedral ($T_d$) coordination, respectively,[25] which is in good agreement with the XANES results that revealed a $Mn^{2+}$ oxidation state in all of the samples. Both manganese crystallographic structures present in the reduced catalysts are illustrated in Figure 10. The relative fractions of MnO and $Ti_2MnO_4$ present in the catalysts can be, moreover, evaluated by the Mn−O coordination numbers, which range from a minimum of 4.0 for a pure $Ti_2MnO_4$ compound to a maximum of 6.0 for pure MnO. Due to the relatively lower X-ray scattering power of Ti[34] and the highly disordered state of the Mn ions, the contribution of Ti to the Fourier transform was not considered in our fitting process. We also note that the Mn−Ti distances in $Ti_2MnO_4$ are 3.57 Å,[25] which are much longer than the distances reported for these catalysts. Hence, the second Mn−Mn shell is merely attributed to the MnO species and decreases in intensity when more $Ti_2MnO_4$ is present in the catalysts. The Mn−Mn coordination numbers are therefore indicative of the fraction of

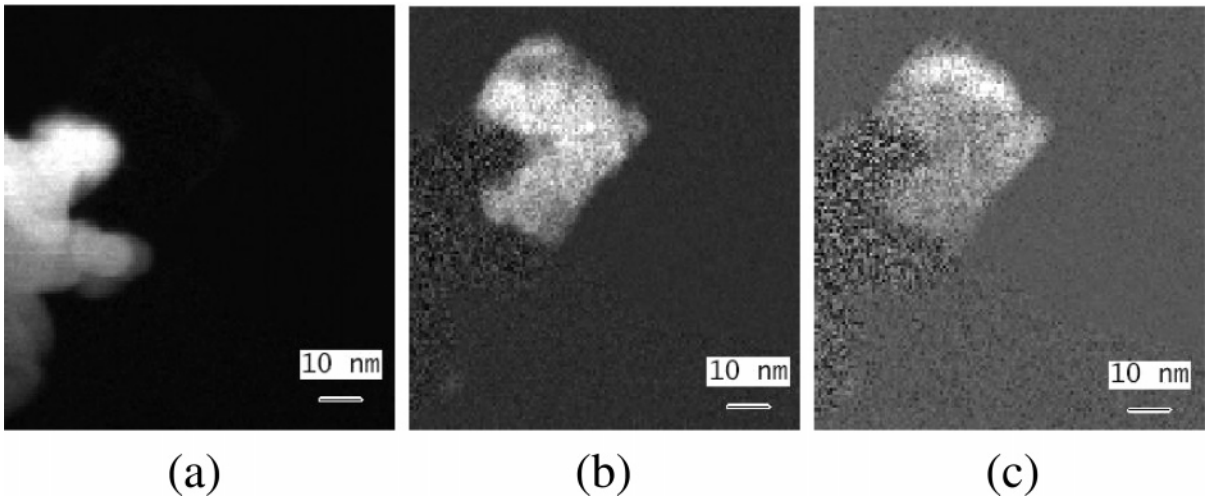


**Figure 11.** Gray-scale EELS Ti L-edge (a), Co L-edge (b), and Mn L-edge (c) chemical maps of the Hcop−CoMn catalyst after reduction and passivation.

manganese in the form of MnO. On the basis of these observations, the amounts of MnO and $Ti_2MnO_4$ in the catalysts reduced at 300 and 350 °C could be estimated.

The lowest coordination number for the Mn−O shell is displayed by the I−CoMn catalyst reduced at 350 °C. In this catalyst, Mn features almost pure 4-fold oxygen coordination (4.1), with distances of 2.04 Å and a very weak Mn−Mn shell at 2.91 Å with only 0.4 Mn neighboring atoms. As already discussed in a previous study,[32] these data reveal that Mn belongs almost entirely to a $Ti_2MnO_4$-type phase. This phase is expected to exist in a highly dispersed state over the $TiO_2$ support, as suggested by the weak Mn−Mn peak and by the relatively flat profile of its XANES spectrum. Similar results were obtained for the I−MnCo sample reduced at 350 °C, although the values suggest that the amount of titanate is slightly lower. This indicates that a variable amount of $Ti_2MnO_4$ is present in all of the reduced catalysts, being in larger amounts after reduction at 350 °C, as indicated by the lower Mn−O and Mn−Mn coordination numbers and the slightly shorter Mn−O bonds. In I−CoMn reduced at 300 °C, the Mn−O distances of 2.09 Å and the Mn−Mn coordination number of 0.9 point towards the presence of more MnO and less $Ti_2MnO_4$ than after reduction at 350 °C. In general, the amounts of MnO in all the IWI catalysts appear to be small, since the Mn exists mostly in the form of $Ti_2MnO_4$.

In contrast, in the Hcop−CoMn catalyst, Mn features nearly a 6-fold coordination with longer interatomic distances (2.15 Å) than all of the other catalysts. Additionally, a second Mn−Mn shell with 11.6 atoms at 3.07 Å has been obtained. Although these data are very similar to the structural parameters of bulk MnO material, the Mn−O and Mn−Mn bond distances (2.15 and 3.07 Å) are significantly shorter than those in the MnO reference material (2.20 and 3.14 Å). These results combined with the XAFS results at the Co K-edge that showed the presence of a pure $Co^{2+}$ oxidation state and the occurrence of longer Co−O and Co−Co bonds than in pure CoO strongly suggest the existence of a MnO−CoO solid solution. Indeed, it is well-known in the literature[35] that since MnO and CoO have similar cubic rock-salt structures, they readily form rock-salt solid solutions of the type $Mn_{1-x}Co_xO$ over a full range of compositions ($0 < x < 1$). Since $Co^{2+}$ is smaller than $Mn^{2+}$, the progressive substitution of $Co^{2+}$ ions in the MnO structure is accompanied by a linear decrease of the cell parameter from 4.446 to 4.263 Å, when $x$ increases in $Mn_{1-x}Co_xO$ from 0 to 1. This would perfectly account for the shortening of the Mn−O and Mn−Mn bonds in the catalyst relative to those in the bulk MnO material. A simulation of the $x$ value in $Mn_{1-x}Co_xO$ corresponding to the bond distances found in Hcop−CoMn (2.15 and 3.07 Å) gives for this catalyst a stoichiometry close to $Mn_{0.25}Co_{0.75}O$.

In H−CoMn reduced at 350 °C, the Mn−O average distance of 2.07 Å and the number of Mn neighboring atoms of 2.3 indicates that the Mn is partly present as $Ti_2MnO_4$ and MnO/$Mn_{1-x}Co_xO$ mixtures. The same catalyst reduced at 300 °C contains more MnO/$Mn_{1-x}Co_xO$ phases, as deduced from the higher Mn−Mn coordination number of 4.3. However, the Mn−O distance remains the same (2.07 Å) regardless of the reduction temperature, suggesting that the amount of $Mn_{1-x}Co_xO$ is increased or the amount of Co incorporated in the solid solution is higher, as a result of the lower Co reduction extent achieved at 300 °C.

The overall results clearly indicate that MnO and $Mn_{1-x}Co_xO$ solid solutions are present in all catalysts to some extent, being less abundant in the IWI catalysts. Nevertheless, the very short Mn−Mn distances (ranging between 2.98 and 3.05 Å) displayed by the IWI catalysts suggest that a large relative amount of cobalt might be mixed with the MnO in the form of $Mn_{1-x}Co_xO$ solutions with a very high value of $x$. These findings reflect the high level of dispersion of the manganese, which exists highly segregated over the catalyst surface in the form of various phases. An exact quantification of these phases, however, has not been attempted, since they are expected to distribute heterogeneously on the catalyst surface. The existence of all the possible manganese species identified by XAFS has been evidenced in a previous work using the STEM-EELS technique.[32,36] Therein, we reported the migration and redispersion of the manganese oxide phase upon reduction, which could be nicely observed in the colored chemical maps obtained with STEM-EELS at the different stages of the activation process.

*3.3. STEM-EELS Analysis of the Reduced Hcop−CoMn Catalyst.* Figure 11 shows the Co, Mn, and Ti EELS chemical maps for the Hcop−CoMn catalyst after $H_2$ reduction at 350 °C. The images exhibit luminosity proportional to the number of given atoms encountered by the electron beam in each subarea and, thus, provide valuable information on the Co, Mn, and Ti elemental distributions in the scanned areas. As the images clearly reveal, the cobalt and manganese are certainly associated in the form of a mixed compound, confirming the formation of $Mn_{1-x}Co_xO$ solid solutions after the reduction treatment. In this

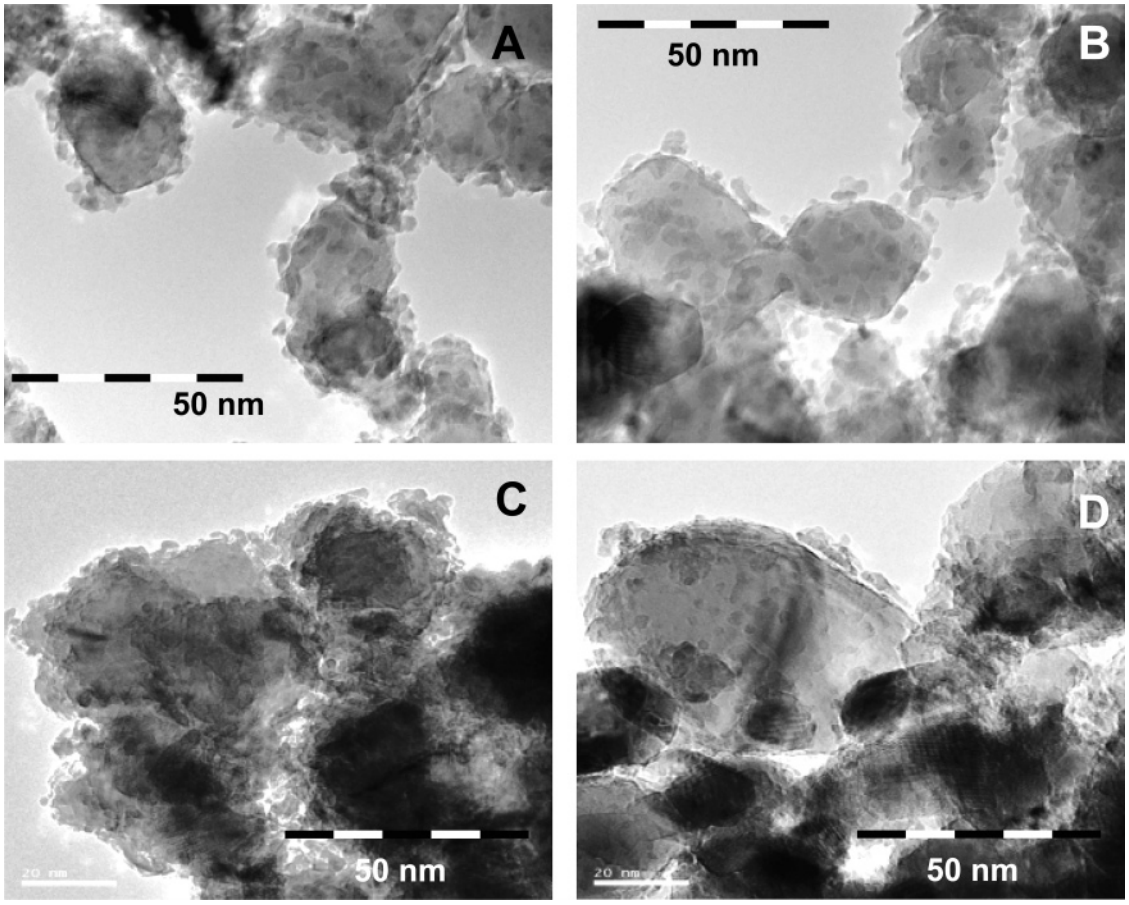


**Figure 12.** TEM images of the I−Co (A and B), I−CoMn (C), and I−MnCo (D) catalysts after reduction at 350 °C in $H_2$/He flow and passivation in $CO_2$ at 150 °C.

example, a large Co/Mn oxide cluster with a peculiar shape can be seen embedded on the $TiO_2$ support.

*3.4. TEM Analysis of Reduced Catalysts.* The effect of the reduction on the cobalt particle size distribution and morphology was studied in the TEM micrographs. The cobalt particles were clearly distinguishable from the $TiO_2$ by the different particle sizes, being of around 2−10 and 30−60 nm, respectively. We note that, as a result of the passivation treatments, the surface of the cobalt particles was reoxidized, and thus, particles smaller than 5 nm are composed merely of CoO, while larger particles may contain a metallic $Co^0$ core and CoO at the outer layer.

Figure 12 presents some TEM images obtained for the IWI catalysts. Very small particles can be nicely seen covering the $TiO_2$ particles and leading to an irregular $TiO_2$ surface. The cobalt is clearly visualized at the edges of the $TiO_2$ particles, and occasionally on top or underneath the $TiO_2$ given by a darker contrast. Figures 12A and 12B show the situation for the I−Co catalyst, in which nearly hemispherical particles of around 2.5−5 nm can be seen covering the $TiO_2$ surface. In the absence of manganese, the cobalt particles appear to have a well-defined shape and are supported on $TiO_2$ without an apparent interaction. Additionally, cobalt is also found in some spots as a highly dispersed thin layer (∼3 nm), as well as forming larger clusters of around 6−8 nm, although to a lesser extent. For I−CoMn and I−MnCo, the cobalt distribution slightly differs from I−Co, as observed in Figures 12C and 12D. These catalysts contain very small particles (∼3−6 nm), as well as some larger agglomerates (∼6−10 nm). Furthermore, the $TiO_2$ surface appears to be less regular most likely as a result of the manganese species highly spread out on the catalyst surface. An estimation of the mean Co particle sizes for the I−Co, I−CoMn, and I−MnCo catalysts resulted in values of 4.3, 4.9, and 4.8 nm, respectively (Table 5). Therefore, the presence of manganese led to the formation of slightly larger cobalt particles.

The TEM results for the HDP catalysts are presented in Figure 13. For the H−Co catalyst (Figures 13A and 13B), very small particles of around 1.5−5 nm can be visualized homogeneously covering the $TiO_2$ surface. The situation resembles that of I−Co, although the cobalt particles are even smaller and more often found in the form of thin layers, leading to a rough catalyst surface. The existence of some amounts of cobalt titanate in this group of catalysts was already suggested by XAFS that revealed lower cobalt reducibility compared to the IWI catalysts. The fraction of the nonreducible cobalt phase is thought to be present in intimate contact with the $TiO_2$, presumably in the form of cobalt titanates, which are known to be hardly reducible.[23] On the other hand, Figures 13C and 13D show that, in the H−CoMn and Hcop−CoMn catalysts, manganese clearly influences the cobalt particle size. These images display larger cobalt clusters in the range 8−15 nm, in addition to smaller particles of around 3−6 nm. For example, several cobalt clusters are indicated by arrows in Figure 13C. These clusters appear to be composed of smaller particles embedded together. Remarkably, small particles are observed for H−CoMn but to a lower extent than for H−Co. Finally, for the Hcop−CoMn catalyst, small cobalt particles were hardly found, while numerous clusters were detected. As an example, Figure 13D shows an image in which a large $TiO_2$ particle is observed and three cobalt clusters of about 10−20 nm are clearly distinguishable at the $TiO_2$ surface, giving a darker contrast. Additionally, other very small black dots are observed on top of the $TiO_2$ particle, indicating the presence of also some small particles.

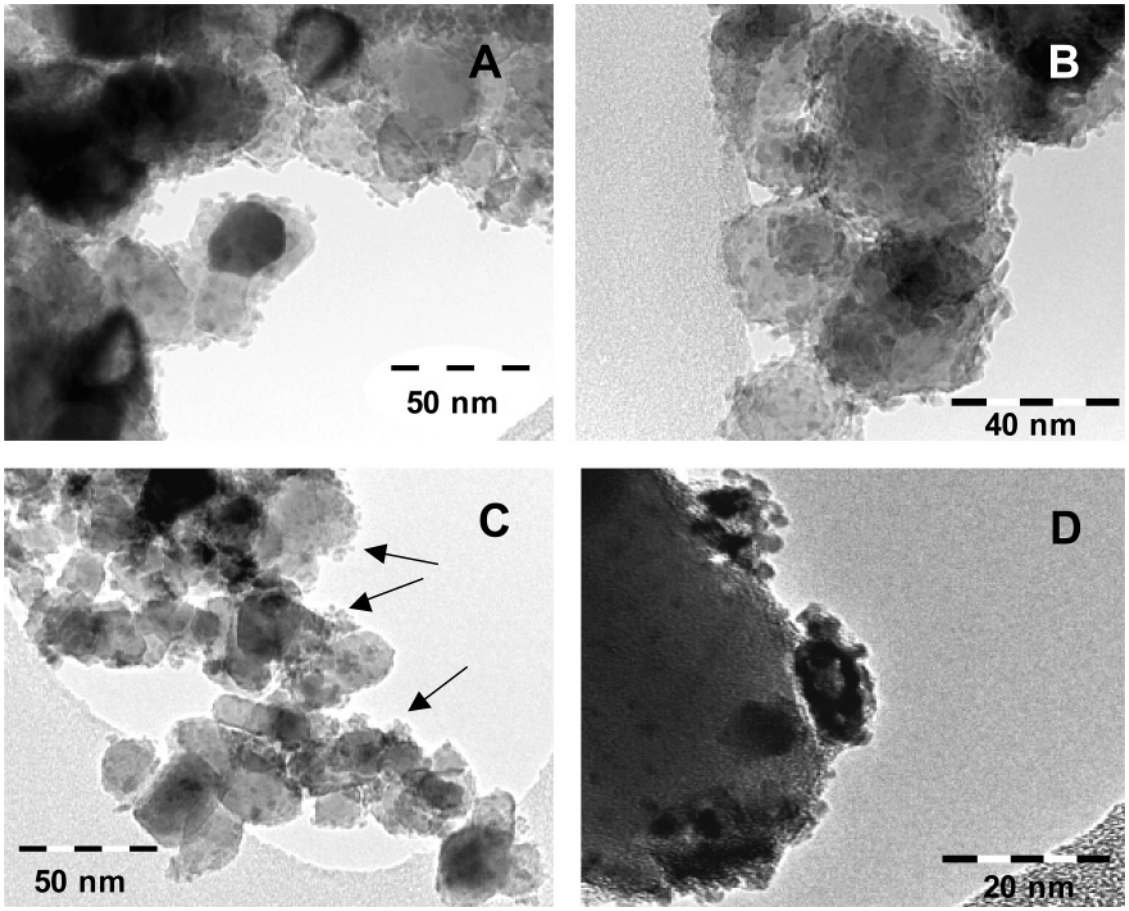


**Figure 13.** TEM images for the H−Co (A and B), H−CoMn (C), and Hcop−MnCo (D) catalysts after reduction at 350 °C in $H_2$/He flow and passivation in $CO_2$ at 150 °C.

The mean Co particle sizes obtained for H−Co, H−CoMn, and Hcop−CoMn were 3.5, 5.6, and 10.5 nm, respectively, reflecting a dramatic influence of manganese on the cobalt particle distribution in the HDP catalysts. This marked influence results from the intimate Co−Mn association that takes place in the catalyst before reduction. Table 5 summarizes the EXAFS and TEM results of the cobalt particle sizes, which turned out to be in good agreement.

**4. Fischer−Tropsch Catalysis.** The evolution of the activity for all of the catalysts during the first 60 h of FT reaction is presented in Figure 14. The IWI catalysts suffer from a rapid deactivation during the first 30 h of reaction, as indicated by the initial drop in activity, after which the Co time yields stabilize in a pseudo-steady state (Figure 14b). It is worthwhile to note that the freshly reduced catalysts are composed of mainly $Co^0$, leading to high $CH_4$ selectivity, whereas during $CO/H_2$ treatments the selectivity to $C_{5+}$ increases in line with the catalyst deactivation. Therefore, this shift in selectivity is ascribed to structural changes of the cobalt surface, which is most likely carburized during the first stage of reaction, thus facilitating the chain growth reaction. Interestingly, the I−Co catalyst deactivates more rapidly and during longer times than I−CoMn and I−MnCo, independently of the reduction temperature. The group of the HDP catalysts also suffers a marked deactivation although only during the first 5 h of reaction (Figure 14b), after which they maintain steady Co time yields. The exception is the H−Co catalyst reduced at 350 °C, which initially displays the highest Co time yields (above $3.0 \times 10^{-5}$ mol of CO (g Co)$^{-1}$ s$^{-1}$) and subsequently deactivates throughout 60 h of reaction. In contrast, the H−CoMn catalyst reduced at 350 °C suffers from a less pronounced deactivation and displays the highest activity among all of the catalysts.

The overall catalytic results are summarized in Table 6. The catalytic performances correspond to a pseudostationary behavior obtained after 60 h of FT reaction. For the IWI catalysts, the highest activities were obtained after reduction at 300 °C, with similar Co time yields of about $(2.31-2.34) \times 10^{-5}$ mol of CO (g Co)$^{-1}$ s$^{-1}$. However, the activities are lower after reduction at 350 °C, with values of 1.64, 1.31, and 2.12 for the I−Co, I−CoMn, and I−MnCo catalysts, respectively. This negative effect observed for the IWI catalysts after reduction at 350 °C is likely related to the presence of small cobalt particles, which are prone to deactivate during reaction as a result of the occurrence of SMSI effects with the $TiO_2$ support.[11,12] SMSI effects are expected to occur at high temperatures, leading to a partial blockage of the small $Co^0$ particles and consequently to a decrease in activity. This phenomenon would also account for the initial drop in activity during the first stage of reaction, since the small particles might deactivate as a result of a reoxidation or site blockage by $TiO_x$. In addition, the activity of I−CoMn is lower than I−Co due the presence of manganese, which might also block some of the small cobalt particles. On the basis of the EXAFS results, this effect may be ascribed to the formation of solid solutions of $Mn_{1-x}Co_xO$ at the surface of cobalt. A similar manganese effect on the activity of SBA-15-supported cobalt catalysts has been reported by Martinez et al.,[37] in which they used a similar range of cobalt dispersions (19−21%) as in our I−CoMn catalyst.

The IWI catalysts are significantly more selective towards the formation of higher hydrocarbons after reduction at 300 °C

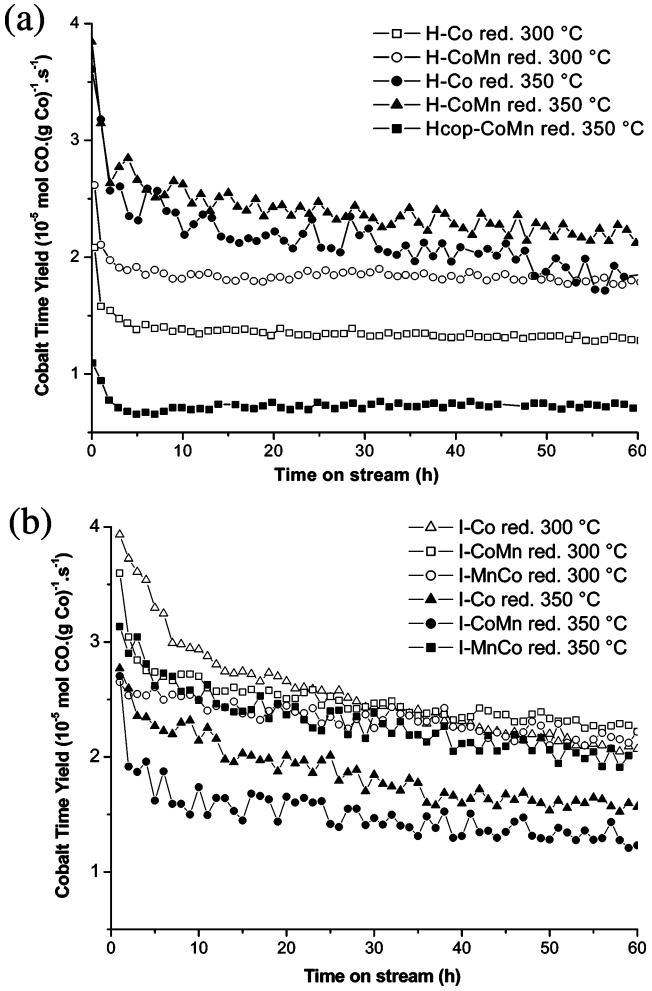


**Figure 14.** Evolution of FT activity during 60 h of reaction of the IWI (a) and HDP (b) catalysts reduced at 300 and 350 °C. The activities are expressed as Co time yield ($10^{-5}$ mol of CO (g Co)$^{-1}$ s$^{-1}$).

**TABLE 6: Overview of the Catalytic Performances of the $Co/TiO_2$ and $Co/Mn/TiO_2$ Catalysts after Reduction at 300 and 350 °C (The Table Includes the Extent of Co Reduction as Measured with XANES)**

| | | | selectivity | | | activity | |
|---|---|---|---|---|---|---|---|
| catalyst | red. temp (°C) | % $Co^0$ reduction | % $CH_4$ | % $C_{5+}$ | α values[a] | Co time yield[b] | TOF[c] |
| I−Co | 350 | 100 | 21 | 48 | 0.69 | 1.64 | 4.28 |
| I−CoMn | 350 | 100 | 21 | 45 | 0.66 | 1.31 | 3.93 |
| I−MnCo | 350 | 100 | 20 | 47 | 0.67 | 2.12 | 6.18 |
| H−Co | 350 | 95 | 32 | 28 | 0.54 | 2.08 | 4.45 |
| H−CoMn | 350 | 90 | 25 | 34 | 0.58 | 2.57 | 8.74 |
| Hcop−CoMn | 350 | ∼5 | 17 | 47 | 0.67 | 0.80 | 5.20 |
| I−Co | 300 | 100 | 17 | 54 | 0.72 | 2.31 | 6.04 |
| I−CoMn | 300 | 48 | 18 | 51 | 0.69 | 2.34 | 7.02 |
| I−MnCo | 300 | 97 | 18 | 51 | 0.69 | 2.32 | 6.68 |
| H−Co | 300 | 40 | 23 | 43 | 0.65 | 1.32 | 2.81 |
| H−CoMn | 300 | ∼5 | 18 | 50 | 0.68 | 1.81 | 6.15 |

[a] As calculated from the slope between $C_3$ and $C_7$ in the ASF distribution plot, according to the equation $\log W_n/n = \log(\ln 2\alpha) + n \log \alpha$, where $W_n$ is the weight fraction of the products with $n$ carbon number. [b] Co time yield: $10^{-5}$ mol of CO (g Co)$^{-1}$ s$^{-1}$. [c] Turnover frequency: $10^{-3}$ s$^{-1}$.

(50−54% $C_{5+}$, 17−18% $CH_4$) than at 350 °C (45−48% $C_{5+}$, 20−21% $CH_4$). A possible explanation for this selectivity decrease may be the formation of smaller unreduced cobalt particles and/or titanate compounds, as previously suggested in the literature.[37,38] On the other hand, no significant differences in product selectivity due to the presence of manganese are found for I−CoMn and I−MnCo, since the I−Co catalyst reduced at 300 °C is the most selective towards the $C_{5+}$ fraction of products and displays the highest chain growth probability (0.72).

For the HDP catalysts, an opposite reduction temperature−activity dependency is found, as shown in Table 6. The highest Co time yields are obtained after reduction at 350 °C, with values of 2.08 and 2.57 × $10^{-5}$ mol of CO (g Co)$^{-1}$ s$^{-1}$ for H−Co and H−CoMn, respectively. Reduction at 300 °C, however, leads to a decrease in activity to values of 1.32 and 1.81 × $10^{-5}$ mol of CO (g Co)$^{-1}$ s$^{-1}$ for the same catalysts. Hcop−CoMn displays the lowest activity (Co time yield of 0.80), reflecting its low cobalt reduction extent. This catalyst did not display any activity after reduction at 300 °C due to the absence of Co metal. Hence, the activity of this group of catalysts is clearly influenced by the cobalt reduction extent, with the activity being proportional to the percentage of $Co^0$. Since the cobalt reduction extent of these catalysts is very low at 300 °C, the formed cobalt particles are expected to remain larger, thereby leading to lower activities. On the other hand, the H−CoMn catalyst displays in all cases higher Co time yields than H−Co, regardless of its larger cobalt particle size and lower reducibility. Remarkably, the TOF numbers after reduction at 350 °C are twice as high in H−CoMn (8.74 × $10^{-3}$ s$^{-1}$) than in H−Co (4.75 × $10^{-3}$ s$^{-1}$). This suggests that cobalt particles larger than 5 nm containing a manganese promoter have a higher intrinsic activity in the FT reaction than small particles as those contained in H−Co. Furthermore, these small particles are more rapidly deactivated during the first stage of reaction.

The selectivity of the HDP catalysts is also largely influenced by the reduction temperature and the presence of manganese. The highest $C_{5+}$ selectivity is obtained for H−CoMn and H−Co reduced at 300 °C, with values of 50 and 43%, respectively. After reduction at 350 °C, the catalysts display lower $C_{5+}$ selectivities of 34 and 28%, respectively. Therefore, a cobalt reduction extent−selectivity dependency is found, since lower reduction extents always result in a higher $C_{5+}$ selectivity. This indicates that a more oxidic cobalt surface composition favors the production of longer hydrocarbon chains in the FT reaction by decreasing the hydrogenation rate leading to $CH_4$ formation. Finally, it is remarkable to notice that the presence of manganese in H−CoMn and Hcop−CoMn leads in all cases to an increase of the chain growth probability and to a decrease of the $CH_4$ production, compared to the Mn-free catalyst. These results clearly show that a manganese promotion has been achieved in the HDP catalysts, leading to important improvements of the FT catalytic performances.

Finally, it is worthwhile to comment on the high $CH_4$ selectivity found for the HDP catalysts after reduction at 350 °C compared to the IWI catalysts. As reported in the literature, the existence of unreduced cobalt species (e.g., titanates or $CoO_x$) is known to catalyze the WGS reaction, thus increasing the effective $H_2/CO$ ratio at the surface of the catalyst.[37−39] Hence, a first explanation for the higher $CH_4$ is the increase of the WGS activity leading to higher hydrogenation rates and, consequently, to a higher $CH_4$ selectivity. The presence of these unreduced phases has been suggested by the XANES analysis. Nevertheless, since the FT experiments were carried out at pressures of 1 bar and low CO conversions (∼3%), the WGS activity may be negligible. Therefore, another possible explanation is that the small cobalt particles provide active sites for the formation of $CH_4$ and not for the polymerization reaction. The existence of very small cobalt particles has been demonstrated by TEM and EXAFS.

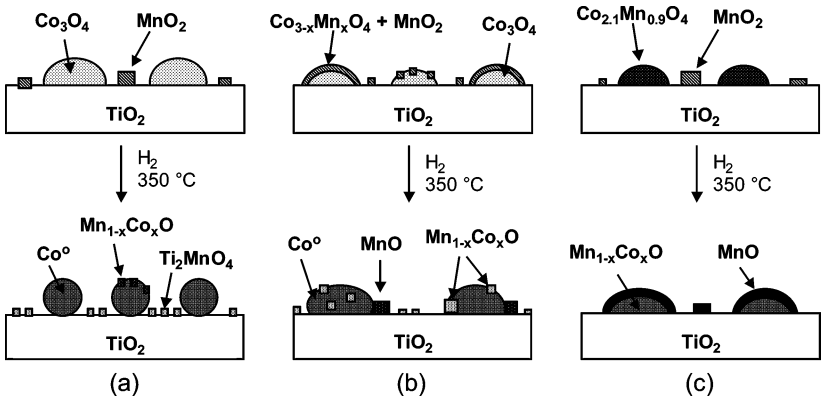


**Figure 15.** Schematic representation of the composition of I−CoMn and I−MnCo (a), H−CoMn (b), and Hcop−CoMn (c) catalysts before and after the reduction treatments.

### Overview of the Molecular Structures and Their Relationship with Fischer−Tropsch Activity

In situ XAFS results at the Co and Mn K-edges in combination with TEM analysis have provided valuable information on the physicochemical properties of the active sites in the catalysts after activation treatments. The preparation method and reduction temperature strongly influenced the chemistry of the cobalt particles and their FT catalytic behavior. We now present an overview of the structural results obtained for the two different groups of $Co/TiO_2$ and $Co/Mn/TiO_2$ catalysts including a more thorough discussion on structure−performance relationships. An overview of the different cobalt and manganese phases present in both groups of $Co/Mn/TiO_2$ FT catalysts before and after reduction is illustrated in Figure 15.

**1. Catalysts Prepared by the Incipient Wetness Preparation.** A first group of $Co/Mn/TiO_2$ catalysts was prepared by the IWI method. These materials after calcination were composed of $Co_3O_4$ clusters of around 20−35 nm and a $MnO_2$ phase dispersed over $TiO_2$ without a marked interaction with $Co_3O_4$. The cobalt phase was fully reduced to $Co^0$ at 350 °C in all cases, ruling out a significant manganese influence on the cobalt reducibility. Remarkably, reduction led to the formation of small cobalt particles in the range 3−6 nm. These particles are orders of magnitude smaller than the initial $Co_3O_4$ clusters, indicating the occurrence of a redispersion of the cobalt phase presumably due to the rupture of the $Co_3O_4$ clusters into smaller aggregates. In this respect, the $TiO_2$ support seems to play a crucial role in stabilizing small metal particles. Thus, a driving force leading to the formation of small $Co^0$ particles may be the occurrence of $Co-TiO_2$ interactions during the reduction process of $Co_3O_4$ to $Co^0$. On the other hand, the presence of manganese did not influence the cobalt dispersion to a great extent.

As a result of the high cobalt dispersion achieved in these catalysts, a drawback is encountered, since the small $Co^0$ particles are not very stable in the FT and consequently display a lower activity than larger particles. According to the literature, $Co^0$ particles in the range 6−200 nm exhibit a similar intrinsic activity for the CO hydrogenation, whereas particles below 6 nm display a lower activity.[40,41] Although the reason for this phenomenon has not been completely elucidated, different explanations have been proposed, such as a reoxidation of small $Co^0$ particles by the $H_2O$ steam or a surface carbide formation. Another plausible cause is the occurrence of SMSI effects, occasionally reported for $TiO_2$-supported catalysts. The occurrence of SMSI may result in a blockage of small $Co^0$ particles by migration of $TiO_x$ overlayers onto the cobalt surface, leading to a decrease in activity.[11,12]

Our results reveal that the IWI catalysts contain cobalt particles smaller than 6 nm and their FT activity is lower after reduction at 350 °C than at 300 °C, suggesting that $TiO_2$ has in this case a negative influence on the activity. Even though EXAFS showed a 100% bulk reduction at 350 °C, the surface of the particles may be covered by $TiO_x$ species, causing the blockage of some active sites and, therefore, a decrease in activity.

Finally, the use of manganese in the IWI catalysts did not significantly benefit the FT catalytic performances. As revealed by XAFS, the manganese exists mainly in the form of a $Ti_2MnO_4$-type phase highly dispersed over the $TiO_2$ surface. Therefore, this phase is not expected to play a significant role in the FT reaction and can be regarded as a spectator species. A small fraction of the manganese was also located at the cobalt surface in the form of $Mn_{1-x}Co_xO$. Taking into account that these catalysts contain very small cobalt particles, the results suggest that manganese does not effectively promote cobalt particles in the range 2−5 nm. On the contrary, a decrease in the activity was occasionally obtained most likely due to the blocking of some active sites by the manganese oxide species.

**2. Catalysts Prepared by Homogeneous Deposition Precipitation.** A second group of $Co/Mn/TiO_2$ catalysts was synthesized by the HDP method and by a combination of the IWI and HDP methods. After calcination, the catalysts were composed of $Co_3O_4$ clusters of around 10−15 nm and a $MnO_2$ phase in intimate contact with the $Co_3O_4$ phase. The cobalt/manganese association resulted in the formation of $Co_{3-x}Mn_xO_4$-type solid solutions, strongly affecting the reduction behavior of these catalysts. Due to the presence of manganese, reduction from $Co_3O_4$ to $Co^0$ was somewhat hampered, with this effect being more severe in the case of high manganese loadings mixed with the cobalt phase. On the other hand, the HDP catalysts were found to not be completely reducible, resulting in lower cobalt reduction extents than the IWI catalysts. The remaining unreduced cobalt is thus thought to exist in a dispersed form in intimate contact with the $TiO_2$ surface (e.g., as titanate or $CoO_x$ species).

The Co particle sizes obtained after reduction were largely influenced by the presence of manganese. While reduction of a $Co/TiO_2$ catalyst resulted in the formation of very small $Co^0$ particles (∼2−4 nm), reduction of $Co/Mn/TiO_2$ catalysts also led to the formation of larger agglomerates (∼8−15 nm). Hence, manganese appears to act as a glue, keeping the cobalt particles in a less segregated state as a result of the decrease in the cobalt reducibility. Therefore, it is considered that manganese when mixed with the cobalt particles may play a role in protecting the cobalt phase against an excessive spreading over $TiO_2$. In this respect, an initial Co−Mn interaction seems to be required in order to obtain this effect.

The size of the cobalt particles was found to strongly influence the FT performances of these catalysts. Remarkably,

the Co/Mn/$TiO_2$ catalyst displayed a higher activity than the Co/$TiO_2$ catalyst at all reduction temperatures employed. Since the Co/$TiO_2$ catalyst has smaller cobalt particles, the results suggest that larger $Co^0$ particles and promoted by manganese oxide have a higher intrinsic activity for the FT reaction. In addition, the stability of the Co/Mn/$TiO_2$ catalysts was also largely improved due to the presence of manganese, since they displayed lower deactivation rates during the first stage of FT reaction.

EXAFS revealed that the manganese phase in the reduced HDP catalysts consists of large amounts of MnO, in addition to some $Ti_2MnO_4$-type phase. This MnO phase was shown to interact with the CoO particles, resulting in rock-salt solid solutions ($Mn_{1-x}Co_xO$), and this formation was enhanced at lower reduction temperatures. Therefore, it seems reasonable that manganese hampers the cobalt reducibility as a result of a mixing between MnO and CoO. These MnO/$Mn_{1-x}Co_xO$ phases turned out to play an important role in the FT catalytic performances, leading to improvements of the $C_{5+}$ selectivity at the expense of $CH_4$ production, which was always suppressed. This shift in selectivity is most likely caused by a decrease in the hydrogenation rate during the reaction, which is indicative of a more oxidized cobalt surface in which the adsorption of $H_2$ is suppressed and the chain growth probability is increased. Manganese in this respect decreases the amount of metallic cobalt surface, resulting in a different favorable termination path of the growing alkyl chain during FT reaction. This promotion effect is obtained as a result of an intimate interaction of the MnO species with the active cobalt particles.

## Conclusions

The synthesis method and pretreatment conditions are key variables affecting the final active site distribution in Co/Mn/$TiO_2$ Fischer−Tropsch catalysts. We found that after calcination the catalysts are composed of $Co_3O_4$ particles and a $MnO_2$ phase, and association is clearly enhanced by the HDP method. The reduction process from $Co_3O_4$ to $Co^0$ leads to a redispersion of the cobalt phase resulting in a decrease of the cobalt particle sizes. An initial association of manganese with the cobalt phase hampers the cobalt reducibility and consequently prevents an excessive spreading of the cobalt phase over the $TiO_2$ surface. On the other hand, $MnO_2$ compounds are easily reduced to $Mn^{2+}$ species, which can either react with the $TiO_2$ surface to form a $Ti_2MnO_4$-type phase or react with the unreduced CoO particles, leading to the formation of rock-salt $Mn_{1-x}Co_xO$-type solutions. The formation of $Ti_2MnO_4$ does not have an apparent influence on the FT catalytic performances and therefore can be regarded as spectator species. In contrast, the formation of $Mn_{1-x}Co_xO$ compounds at the surface of the $Co^0$ particles can benefit both the activity and selectivity of the catalysts. In this respect, large cobalt particles are required in order to achieve this promotion effect, since small cobalt particles are prone to being covered and blocked by $MnO_x$ and/or $TiO_x$ species, resulting in a lower number of active sites for the FT reaction. In other words, manganese oxide promotion effects are largely influenced by the preparation method and pretreatment conditions and are only experimentally observable in well-defined cases.

**Acknowledgment.** For financial support, we thank Shell Global Solutions and the Utrecht University XAFS user support group. Access to the synchrotron facilities at the ESRF (BM26 DUBBLE-experiment 26-01-191) was arranged through the general support of NWO, and we wish to acknowledge the assistance and advice of Sergey Nikitenko during the XAS measurements. Cor van der Spek and Alex Glotter are kindly acknowledged for the TEM and STEM-EELS measurements, respectively. The work has benefited from fruitful discussions with H. Oosterbeek, H. Kuipers, and C. Mesters of Shell Global Solutions.

## References and Notes

(1) Dry, M. E. *Catal. Today* **2002**, *71*, 227.
(2) Schulz, H. *Appl. Catal., A* **1999**, *186*, 3.
(3) Shell press release on March 9, 2004 (http://www.shell.com).
(4) http://www.sasol.com.
(5) Exxon Mobil press released on July 14, 2004 (http://www.exxon-mobil.com).
(6) Fu, L.; Bartholomew, C. H. *J. Catal.* **1985**, *92*, 376.
(7) Lee, J. H.; Lee, D. K.; Ihm, S. K. *J. Catal.* **1988**, *113*, 544.
(8) Iglesia, E.; Soled, S. L.; Fiato, R. A. *J. Catal.* **1992**, *137*, 212.
(9) Schulz, H.; Nie, Z.; Ousmanov, F. *Catal. Today* **2002**, *71*, 351.
(10) Jacobs, G.; Patterson, P. M.; Zhang, Y.; Das, T. *Appl. Catal., A* **2002**, *233*, 215.
(11) Vannice, M. A. *J. Catal.* **1982**, *74*, 199.
(12) Haller, G. L.; Resasco, D. E. *Adv. Catal.* **1989**, *36*, 173.
(13) Barrault, J. *Stud. Surf. Sci. Catal.* **1982**, *11*, 225.
(14) Van der Riet, M.; Copperthwaite, R. G.; Hutchings, G. J. *J. Chem. Soc., Faraday Trans.* **1987**, *83*, 2963.
(15) Riedel, T.; Cleys, M.; Schulz, G.; Schaub, G.; Nam, S.; Jun, K.; Choi, M.; Kishan, G.; Lee, K. *Appl. Catal., A* **1999**, *186*, 201.
(16) Keyser, M. J.; Everson, R. C.; Espinoza, R. L. *Appl. Catal., A* **1998**, *171*, 99.
(17) Kölbel, H.; Engelhard, F. *Erdoel Kohle* **1949**, *2*, 52.
(18) Goes, M. F.; Rek, P. J. M.; Schaddenhorst, D.; Lange, J.-P.; Geerlings, J. J. C.; Oosterbeek, H. U.S. Patent 5,981,608, 1999.
(19) Vaarkamp, M.; Mojet, B. L.; Kappers, M. J.; Miller, J. T.; Koningsberger, D. C. *J. Phys. Chem.* **1995**, *99*, 16067.
(20) Binsted, N.; Campbell, J. W.; Gurman, S. J.; Stephenson, P. C. *EXAFS Analysis Programs*; Warrington, U.K., 1991.
(21) Stephan, O.; Gloter, A.; Imhof, D.; Kociak, M.; Suenaga, K.; Tence, M.; Colliex, C. *Surf. Rev. Lett.* **2000**, *7*, 475.
(22) Rios, E.; Chartier, P.; Gautier, J. L. *Solid State Sci.* **1999**, *1*, 267.
(23) Brik, Y.; Kacimi, M.; Ziyad, M.; Bonzon-Verduraz, F. *J. Catal.* **2001**, *202*, 202.
(24) Kim, K. J.; Park, Y. R. *Solid State Commun.* **2003**, *127*, 25.
(25) Fletcher, D. A.; McMeeting, R. F.; Parking, D. *J. Chem. Inf. Comput. Sci.* **1996**, *36*, 746.
(26) Naka, S.; Inagaki, M.; Tanaka, T. J. *Mater. Sci.* **1972**, *7*, 441.
(27) Gautier, J. L.; Rios, E.; Gracia, M.; Marco, J. F.; Gancedo, J. R. *Thin Solid Films* **1997**, *311*, 51.
(28) Wells, A. F. *Structural Inorganic Chemistry*, 5th ed.; Clarendon Press: Oxford, U.K., 1984.
(29) Martin de Vidales, J. L.; Vila, E.; Rojas, R.; Garcia-Martinez, O. *Chem. Mater.* **1995**, *7*, 1716.
(30) Vila, E.; Rojas, R. M.; Vidales, J. L.; Garcia-Martinez, O. *Chem. Mater.* **1996**, *8*, 1078.
(31) Ciuparu, D.; Haider, P.; Fernandez-Garcia, M.; Chen, Y.; Lim, S.; Haller, G. L.; Pfefferle, L. *J. Phys. Chem. B* **2005**, *109*, 16332.
(32) Morales, F.; Grandjean, D.; de Groot, F. M. F.; Stephan, O.; Weckhuysen, B. M. *Phys. Chem. Chem. Phys.* **2005**, *7*, 568.
(33) Liang, Q.; Chen, K.; Hou, W.; Yan, Q. *Appl. Catal., A* **1998**, *166*, 191.
(34) Bartholomew, C. H.; Reuel, R. C. *Ind. Eng. Chem.* **1985**, *24*, 56.
(35) Jimemez Mateos, J. M.; Morales, J.; Tirado, J. L. *Thermochim. Acta* **1988**, *133*, 257.
(36) Morales, F.; de Groot, F. M. F.; Gijzeman, O. L. J.; Mens, A.; Stephan, O.; Weckhuysen, B. M. *J. Catal.* **2005**, *230*, 301.
(37) Martinez, A.; Lopez, C.; Marquez, F.; Diaz, I. *J. Catal.* **2003**, *220*, 486.
(38) Reuel, R. C.; Bartholomew, C. H. *J. Catal.* **1984**, *85*, 78.
(39) Johnson, B. G.; Bartholomew, C. H.; Goodman, D. W. *J. Catal.* **1991**, *128*, 231.
(40) Bartholomew, C. H.; Reuel, R. C. *Ind. Eng. Chem. Prod. Res. Dev.* **1985**, *24*, 56.
(41) Bezemer, G. L.; Bitter, J. H.; Kuipers, H. P. C. E.; Oosterbeek, H.; Holewijn, H.; Xu, X.; Kapteijn, F.; van Dillen, A. J.; de Jong, K. P. *J. Am. Chem. Soc.* **2006**, *128*, 3956.